Nanoscale Advances

ROYAL SOCIETY OF CHEMISTRY

REVIEW

View Article Online
View Journal | View Issue

Cite this: *Nanoscale Adv.*, 2025, **7**, 700

Efficient counter electrode for quantum dot sensitized solar cells using p-type PbS@reduced graphene oxide composite†

Huu Phuc Dang, *[a] Ha Thanh Tung,[b] Nguyen Thi My Hanh,[cde] Nguyen Thuy Kieu Duyen,[f] Vo Thi Ngoc Thuy,[cd] Nguyen Thi Hong Anh[g] and Le Van Hieu [dh]

This study developed a novel PbS–rGO composite counter electrode to enhance the performance of quantum dot-sensitized solar cells (QDSSCs). The composite was synthesized *via* a hydrothermal method by anchoring PbS nanocubes onto reduced graphene oxide (rGO) sheets. The effect of the mass ratio of rGO to PbS (0.0, 0.1, 0.3, and 0.6) on power conversion efficiency (PCE) was investigated. The optimized rGO–PbS (0.03) composite achieved a power conversion efficiency of 5.358%, V_{oc} of 0.540 V, J_{sc} of 21.157 mA cm^{-2}, and FF of 0.516. The rGO framework provides an interconnected conductive network that facilitates efficient charge transport, reduces charge transfer resistance, and improves overall conductivity. Electrochemical analyses confirmed the superior electrocatalytic activity of the composite in reducing the S_n^{2-}/S^{2-} redox couple. The unique band alignment between rGO and PbS optimized the electron transfer pathways. The hierarchical structure increased the surface area and light absorption, enabling a more effective charge transfer at the electrode–electrolyte interface.

Received 22nd November 2024
Accepted 24th December 2024

DOI: 10.1039/d4na00971a

rsc.li/nanoscale-advances

1. Introduction

Solar energy, commonly regarded as a clean, abundant, cost-effective, and low-polluting energy source, has attracted substantial attention as a rapidly expanding and affordable power source.[1] Third-generation solar cells, including polymer solar cells (PSC),[2] dye-sensitized solar cells (DSSC),[3] quantum dot solar cells (QDSCs),[4] perovskite solar cells,[5] and hybrid solar cells,[6] have gained interest because of their cost-effectiveness compared with prior generations of solar cells. Quantum dot (QD)-sensitized solar cells (QDSSCs) have garnered significant attention among the third-generation solar cell technologies. This interest stems from the ability to physically adjust the bandgap of QD materials, which offers the potential to surpass the Shockley–Queisser limit.[7,8] The sandwich structure of QDSSCs comprises three main components: a photoanode with quantum dot sensitizers attached to TiO_2, an electrode on the opposite side, and an electrolyte containing redox-active species. In electrochemical systems, the counter electrode serves a critical function by extracting electrons from the photoanode and enabling the reduction reaction at the electrode–counter electrode boundary. For optimal performance, an effective counter electrode must demonstrate several essential properties, including superior catalytic capabilities, excellent electrical conductivity, and robust resistance to both chemical and mechanical stresses. The efficiency of a traditional Pt CE can be hindered by the adsorption of polysulfides on its surface, which restricts its catalytic efficiency in a polysulfide redox couple system.[9] Research on non-platinum CE has explored alternative materials, such as metal chalcogenides, conductive polymers, and carbon-based materials, to address this issue. Metal chalcogenides, including CoS,[10] MoS_2,[11] NiS,[12] CuS,[13] Cu_2S,[14,15] PbS,[16] and CuS/PbS,[17,18] have shown good electrocatalytic activity for the polysulfide redox couple. In particular, PbS has demonstrated exceptional catalytic activity and chemical and electrochemical stability.[19,20] Additionally, its narrow bandgap allows it to absorb residual red or infrared light penetrating the photoanode, resulting in a quasi-Fermi shift

[a]*Faculty of Fundamental Science, Industrial University of Ho Chi Minh City, No. 12 Nguyen Van Bao, Ward 4, Go Vap District, Ho Chi Minh City, 700000, Vietnam. E-mail: danghuuphuc@iuh.edu.vn*

[b]*Faculty of Basic Sciences, Vinh Long University of Technology Education, Vinh Long City, Vietnam*

[c]*Faculty of Physics & Engineering Physics, VNUHCM-University of Science, Ho Chi Minh City, Vietnam*

[d]*Vietnam National University Ho Chi Minh City, Ho Chi Minh City, Vietnam*

[e]*Faculty of Mechanical Engineering, Industrial University of Ho Chi Minh City, No. 12 Nguyen Van Bao, Ward 4, Go Vap District, Ho Chi Minh City, 700000, Vietnam*

[f]*Faculty of Chemical Engineering, Industrial University of Ho Chi Minh City, Ho Chi Minh, Vietnam*

[g]*Faculty of Chemical Engineering, Ho Chi Minh City University of Industry and Trade, 140 Le Trong Tan Street, Tay Thanh Ward, Tan Phu District, Ho Chi Minh City, 70000, Vietnam*

[h]*Faculty of Materials Science and Technology, University of Science, VNU–HCMC, Ho Chi Minh City, Vietnam*

† Electronic supplementary information (ESI) available. See DOI: https://doi.org/10.1039/d4na00971a

towards the vacuum Fermi level under illumination.[21] This strategy has the potential to enhance V_{oc} without compromising the J_{sc}. Additionally, PbS possesses relatively low conductivity, which can result in considerable charge transfer resistance at the counter electrode, ultimately culminating in a low fill factor (FF).[22] Nevertheless, potential solutions exist to enhance the conductivity within the active layer, such as annealing the film or incorporating conductive materials that exhibit superior conductivity.[21]

Materials composed of carbon, such as carbon nanotubes, carbon black, graphene, porous carbon, and activated carbon, provide numerous benefits. These advantages encompass affordability, comparative resilience, and superior electrical conduction properties.[23,24] However, the limited number of active sites on the sp^2 carbon framework is not effective in reducing S_n^{2-}, leading to insufficient performance of QDSSC based on carbon CE.[25] Therefore, composite counter electrodes have the potential to address some of the limitations associated with conventional counter electrodes. According to Parand *et al.* (2014), a graphene/PbS composite was used as the counter electrode, resulting in a performance level 2.63% higher than that of a pristine PbS counter electrode (1.28%).[26] Yang *et al.* (2012) prepared PbS/carbon black (CB) counter electrodes using a solvothermal process, and a catalyst coated on FTO using a polyvinylidene fluoride (PVDF) binder. A quantum dot solar cell utilizing CdS/CdSe/TiO_2 and PbS/CB composite counter electrodes achieved a power conversion efficiency (PCE) of 3.71%.[27] Samadpour *et al.* prepared a graphene/CuS/PbS CE nanocomposite. The PCE of the CdS/CdSe QD-sensitized cells and graphene/CuS/PbS Ces was 3.21%, which was higher than that of the CuS/PbS CEs by 2.54%.[28] Pei *et al.* (2019) prepared PbS quantum dots decorated on MWCNTs@Ti meshes using the successive ionic layer adsorption and reaction (SILAR) technique. The quantum dot solar cells (QDSCs) utilizing PbS/MCNT as counter electrodes achieved photovoltaic conversion efficiencies up to 6.39%, surpassing those of pure MWCNT CE by approximately 40%.[29] Among carbon materials, reduced graphene oxide (rGO) possesses a higher specific surface area, porosity, and electrical conductivity than graphene and carbon black,[30,31] surpassing those of carbon nanotubes (CNTs).[31] As a two-dimensional carbonaceous material, rGO can form templates and networks, which allow it to function as a conduit for charge transfer. After an extensive review of the literature, it was concluded that the combination of PbS with rGO substantially improves the efficiency of the electrocatalyst.

This study developed a novel PbS–rGO composite counter electrode to enhance the performance of quantum dot-sensitized solar cells (QDSSCs). The composite was synthesized *via* a hydrothermal method by anchoring PbS nanocubes onto reduced graphene oxide (rGO) sheets. The rGO framework provides an interconnected conductive network that facilitates efficient charge transport, reduces charge transfer resistance, and improves overall conductivity. The unique band alignment between rGO and PbS optimized the electron transfer pathways. The hierarchical structure increased the surface area and light absorption, enabling a more effective charge transfer at the electrode–electrolyte interface.

2. Material and method

Photocathode graphene oxide (GO), polyvinylpyrrolidone (PVP) $(C_6H_9NO)_n$, thiourea $SC(NH_2)_2$, ethylene glycol $(CH_2OH)_2$, lead(II) nitrate $(Pb(NO_3)_2)$, polyethylene glycol (PEG) $(C_6H_9NO)_n$, selenium (Se), sodium sulfite (Na_2SO_3), sodium hydroxide (NaOH), cadmium acetate dihydrate $(CH_3COO)_2Cd\cdot 2H_2O$, copper(II) chloride $(CuCl_2\cdot 2H_2O)$, zinc nitrate hexahydrate $(Zn(NO_3)_2\cdot 6H_2O)$, and sodium sulfide nonahydrate $(Na_2S\cdot 9H_2O)$ were purchased from Sigma Aldrich. Methanol (CH_3OH), ethanol (C_2H_6O), sulfur (S), acid chloride (HCL), and potassium chloride (KCl) were purchased from Aladdin Reagent Co. Ltd. Titania paste (43T mesh) and fluorine-doped tin oxide glass (FTO, 7 Ω sq^{-1}) were commercially available from Dyesol.

Fabrication of photoanode FTO/TiO_2/CdS/CdSe: Cu/ZnS

The method for fabricating photoanodes using the sequential ion layer adsorption and reaction (SILAR) technique is thoroughly described in this section. The FTO glass was cleaned using a multistep ultrasonic method with acetone, ethanol, and deionized water. Subsequently, a TiO_2 film was coated onto the FTO glass using a screen-printing technique. The FTO/TiO_2 films were dried at 80 °C for 30 min and annealed at 450 °C for 30 min. After sintering, CdS and Cu^{2+} ion-doped CdSe (Cd^{2+}/Cu^{2+} molar ratio = 0.3) quantum dots were deposited on the TiO_2 film using the SILAR method. The SILAR cycle for CdS synthesis included FTO/TiO_2 glass vertically immersed in a Cd^{2+} ion solution for 5 min and then rinsed with ethanol. Subsequently, the FTO/TiO_2 glass was soaked in an S^{2-} ion solution for 5 min and rinsed with methanol. The FTO/TiO_2/CdS photoanode was immersed in a beaker containing a Cd^{2+} : Cu(0.3) ion solution and subsequently rinsed with ethanol to fabricate the FTO/TiO_2/CdS/CdSe : Cu(0.3) electrode. After immersing the electrode in an ion Se^{2-} solution at 70 °C, it was rinsed with distilled water and dried at room temperature. A FTO/TiO_2/CdS/CdSe : Cu(0.3) electrode was developed after three SILAR cycles. The preparation of Cd, S, and Se precursor solutions adhered to the documents cited in the literature.[32] A ZnS surface passivation layer was then deposited using the SILAR method, with 0.1 M $Zn(NO_3)_2$ and 0.1 M Na_2S dissolved in ethanol. The photoanode was subsequently washed with ethanol and stored in the dark under inert gas for further use.

Fabrication of photocathode FTO/rGO–PbS

Two-step hydrothermal and screen-printing methods were employed to fabricate the PbS/rGO composite counter electrode (CE). Lead nitrate and thiourea were utilized as precursors for Pb and S, respectively, whereas ethylene glycol (EG) and PVP served as surfactants. Initially, thiourea and $Pb(NO_3)_2$ were stirred slowly at room temperature until complete dissolution was achieved. Next, 20 ml of ethylene glycol (EG) and 0.5 g PVP were introduced into the solution and magnetically stirred until the PVP completely dissolved. The resulting mixture was then transferred to a 100 ml Teflon container and subjected to hydrothermal treatment at 180 °C for 24 h. An identical procedure was employed to prepare rGO-embedded PbS composites.

During the synthesis of rGO-embedded PbS, 24 mg of graphene oxide and 8 ml ethanol were added to the final product, and the hydrothermal reaction was conducted as previously described. The mass ratios of rGO to PbS were 0.1, 0.3, and 0.6. The samples are denoted as rGO–PbS (x) (x = 0.1, 0.3, and 0.6). A homogeneous viscous mixture was created by mixing the prepared sample with 10 ml of ethanol and 1.2 g PEG in a beaker. This mixture was coated onto an FTO substrate using screen printing techniques, resulting in a CE with an active area of 0.25 cm^2. The final step involved heat treating the FTO/PbS–rGO film at 350 °C for 30 min (Scheme 1).

Assembly of QDSSCs

The photoanode and CE were sealed with Surlyn packing film and filled with a redox electrolyte of 2 M Na_2S, 2 M S, and 0.2 M KCl, resulting in an active area of 0.25 cm^2 for the cell.

Measurements and characterizations

X-ray diffraction (XRD) patterns of the nanocomposites were acquired using a Bruker D8 Advance. High-resolution transmission electron microscopy (HRTEM) images and selected-area X-ray diffraction (XRD-SAED) patterns of the nanocomposites were obtained using a JEM 2100 electron microscope (JEOL, Tokyo, Japan). The morphological characteristics of the nanocomposites were examined using field-emission scanning electron microscopy (FESEM) S-4800 (Hitachi, Japan). Additionally, the elemental composition of the nanocomposites was investigated using electron dispersive X-ray spectroscopy (EDX) attached to the SEM instrument. A Horiba (XploRA PLUS) spectrometer was used to record the Raman spectra at an incident laser light wavelength of 532 nm. Electrochemical impedance spectroscopy (EIS) and cyclic voltammetry (CV) were performed using a potentiostat/galvanostat (CHI 650E electrochemical workstation). The current–voltage (J–V) curve of the quantum dot solar cell (QDSSC) was measured using a source meter (Keithley 2450) under a standard solar irradiance of 300 W m^{-2} (using an Xe lamp with an AM 1.5 filter).

3. Result and discussion

The crystallinity of the PbS crystals decorated on the rGO sheets was determined by X-ray diffraction (XRD) (Fig. 1). The diffraction peak of the rGO powder is observed at 25.9°, which is related to the (002) plane. PbS and PbS–rGO-x nanocomposites

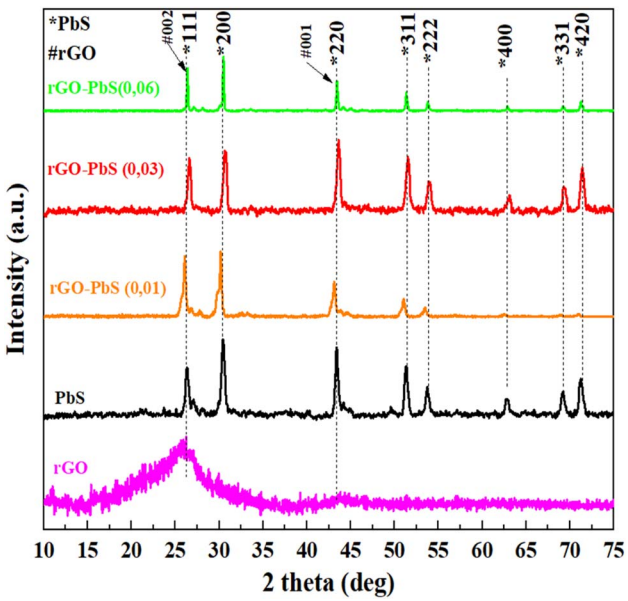

Fig. 1 XRD patterns of rGO, PbS, rGO–PbS x (x = 0.01, 0.03, 0.06) nanocomposites.

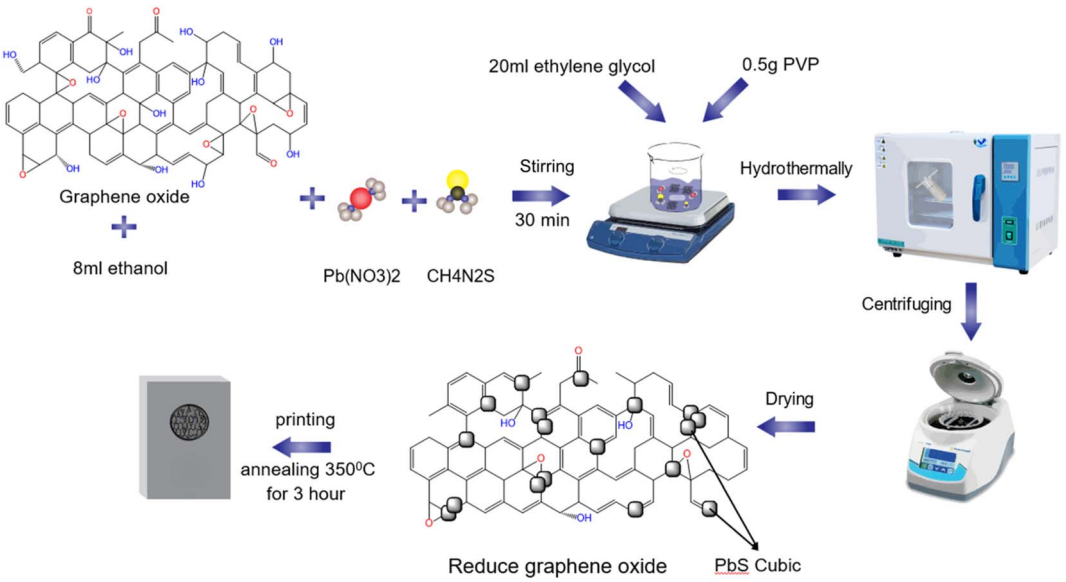

Scheme 1 Synthesis of the FTO/PbS–rGO counter electrode.

have diffraction peaks at 25.93°, 30.06°, 43.02°, 50.99°, 53.41°, 62.52°, 68.85° and 70.93° with (111), (200), (220), (311), (222), (400), (331), (420) faces. These results indicate typical cubic PbS phase crystals (JCPDS card # 01-078-1054). According to the XRD results, the diffraction peak intensity at 30.06° represented the (200) lattice surface with the highest line. The findings presented above indicate that the hydrothermal method successfully yielded rGO–PbS nanocomposites.

Raman spectroscopy was employed to investigate the structural characteristics of the PbS nano cubic and rGO–PbS (x) nanocomposites. Raman spectroscopy revealed two peaks at 271 and 967 cm^{-1} in the PbS sample, indicating bonding between Pb and S.[33] Two additional 431 and 602 cm^{-1} peaks belong to longitudinal optical phonons (LO and three LO, respectively).[34] Meanwhile, the PbS peaks of the rGO–PbS (x) nanocomposites show a blue shift compared to the PbS nanocubic owing to the interaction between rGO and PbS. In the rGO–PbS (x) nanocomposites, the band at ~1342 cm^{-1} (D band) was found to be associated with damage to the graphene lattice structure when subjected to high-temperature reduction.[35] The band at 1576 cm^{-1} (G band) shows the reproduction of sp^2 hybridization between carbon bonds.[24] The D peak intensities of all rGO–PbS (x) nanocomposites were lower than the G peak intensity, and the I_D/I_G intensity of all samples was less than 1, which demonstrates the low defects and reproducibility of bonds between carbon atoms in the rGO network structure during the hydrothermal cutting process at high temperatures. Furthermore, the broad 2D peak (Fig. 2b) observed at approximately 2692 cm^{-1} indicates the formation of multilayered reduced graphene oxide (rGO) sheets separated by lead sulfide (PbS) nanoparticles. The stacked rGO sheets exhibited sp^2 hybridization and provided a facile lateral pathway for electron conduction, potentially reducing the series resistance of the electrodes.

The results of the Fourier transform infrared (FT-IR) spectroscopy analysis of the functional groups present in GO, rGO, and PbS–rGO (x) are illustrated in Fig. 3. The FT-IR spectrum of GO (Fig. 3) shows functional groups C–O (1048 cm^{-1}), C–O–C (1223 cm^{-1}), C–OH (1376 cm^{-1}), and C=C (1634 cm^{-1}), as well as a broad peak between 3000 and 3500 cm^{-1} corresponding to O–H vibration.[36–38] Additionally, the spectral peak observed at 1725 cm^{-1} is associated with the C=O bond vibrations of the carboxylic acid and carbonyl groups. These functional groups are predominantly located at the edges of the graphene sheets, although they can also be found on the basal planes of the sheets.[37] These functional groups were either reduced or decomposed by the thermal reduction of GO, as evidenced by the FTIR spectrum of rGO. The FT-IR analysis (Fig. 3) indicated that GO was successfully reduced by thermal reduction. The FT-IR spectrum of PbS displays well-defined peaks at approximately 600 and 1076 cm^{-1}, which are assigned to S–S stretching vibrations[39] and the frequency of the heteropolar diatomic molecules of PbS,[40] respectively. Additionally, there is a blue shift in some Pb–S groups compared to PbS alone, as well as the

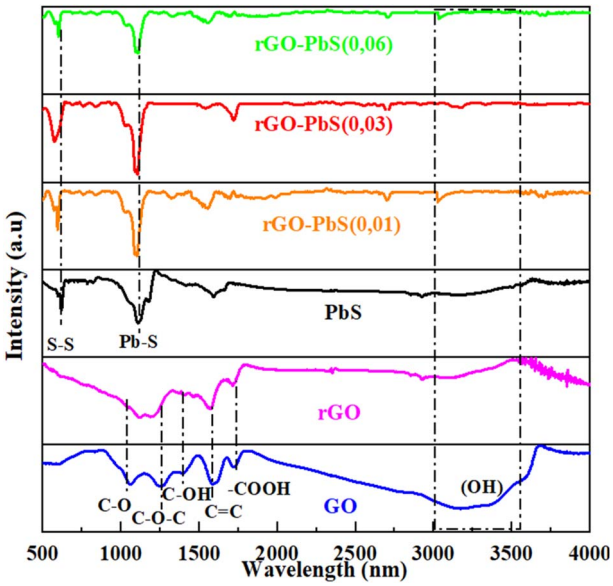

Fig. 3 FT-IR of PbS, GO, rGO, and rGO–PbS (x) (x = 0.01, 0.03, 0.06) nanocomposites.

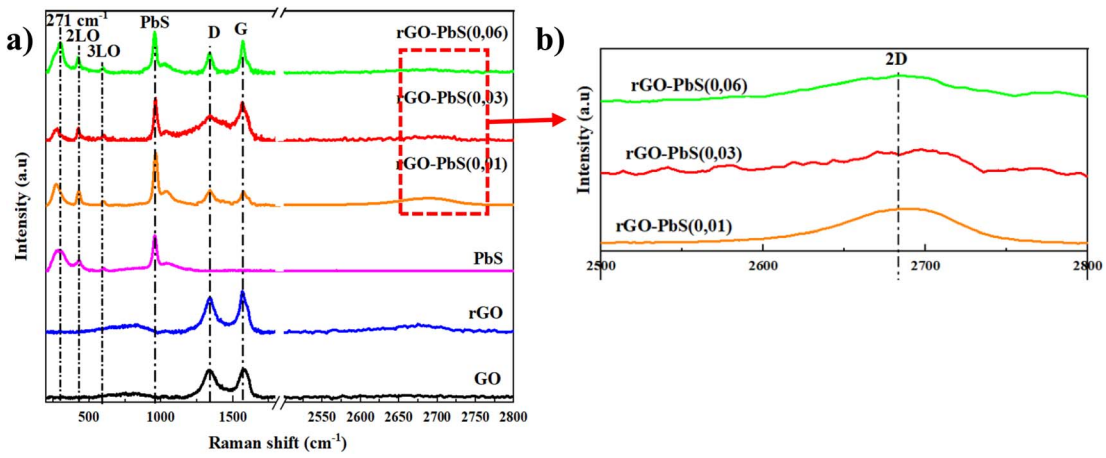

Fig. 2 (a) Raman spectrum of PbS, GO, rGO, and rGO–PbS (x) (x = 0.01, 0.03, 0.06) nanocomposites; (b) inset Raman spectrum in range 2500–2800 cm^{-1}.

incorporation of the chloride group in the composite, which was a result of interactions between the constituents of the formed composite.

The morphology of PbS is shown in Fig. 4a, and the PbS crystal grains are cubic with sharp cubic angles. In addition, some PbS crystals growing on top of each other are of different sizes. For rGO–PbS structures with rGO/PbS ratios of 0.01, 0.03, and 0.06 (Fig. 4a–c), we observed a cubic nanocrystalline morphology. PbS, rGO sheets with large, stacked arrays (yellow circles), and PbS attached to the rGO sheets. The rGO/PbS ratio was 0.06 (Fig. 4d), and more PbS nano-cubic particles were attached to the rGO sheets than 0.01 (Fig. 4b) and 0.03 (Fig. 4c). The cubic structure of PbS crystals is thought to enable effective charge transfer, enhancing the rate of charge diffusion within the electrolyte solution and consequently boosting electricity density. Arranged in distinct patterns, the rGO sheets (indicated by red circles) serve as frameworks that support and contain PbS crystalline particles.

X-ray dispersive spectrum analysis confirmed the presence and percentage of elements in the rGO–PbS 0.03 composite CE (Fig. 5). Fig. 5a shows the presence of carbon (C), oxygen (O), lead (Pb), and sulfur (S) elements. The peak energies of Pb and S were identified at the Mα and Lα lines of Pb at 2.34 and 10.55 keV, and the Kα line of S at 2.30 keV. In addition, Fig. 5b and the inset table show the composition of the PbS FTO/rGO, where the Pb-to-S atomic ratio was approximately 1.05, corresponding to the PbS structure.

Fig. 6a and b present TEM images of the rGO–PbS composite (0.03), which show PbS nano cubic crystal particles embedded in the rGO sheets. Fig. 6c and d show high-resolution Temp (HRTEM) images showing lattice fringes with *d*-spacing of 0.35 nm, and 0.352 nm corresponding to the 002 plane of rGO and the 111 plane of PbS, respectively.

The chemical state of the FTO/rGO–PbS 0.03 counter electrode (CE) was examined using X-ray photoelectron spectroscopy (XPS) to verify the material's composition and bonding characteristics. Fig. 7a and 8b depict the high-resolution C 1s spectra for GO and rGO/PbS, respectively. The C 1s peak in both spectra was deconvoluted into three main components: C–C bond at ~284.6 eV, representing sp^2 hybridized carbon, C–O bond (C–OH, C–O–C) at 286.7 eV, associated with oxygen-bearing functional groups, and C=O bond (O–COH) at 288.1 eV, attributed to carboxylic and carbonyl groups.[41,42] After the reduction of GO, a significant decrease in the intensity of the C–O–C component at 286.7 eV was observed, indicating the effective removal of oxygen-containing functional groups. This transformation demonstrates the successful reduction of GO to rGO, partially restoring the sp^2 carbon network, which is critical for enhanced electrical conductivity in counter electrodes.[42] The Pb 4f spectrum (Fig. 7c) revealed two prominent peaks: 139.0 eV (Pb $4f_{7/2}$) and 143.8 eV (Pb $4f_{5/2}$), confirming the presence of Pb^{2+} ions in the PbS nanoparticles. This indicates the successful integration of PbS into the counter-electrode matrix.[9] The S 2p spectrum (Fig. 7d) exhibited: peaks at 161.6 eV (S $2p_{3/2}$) and

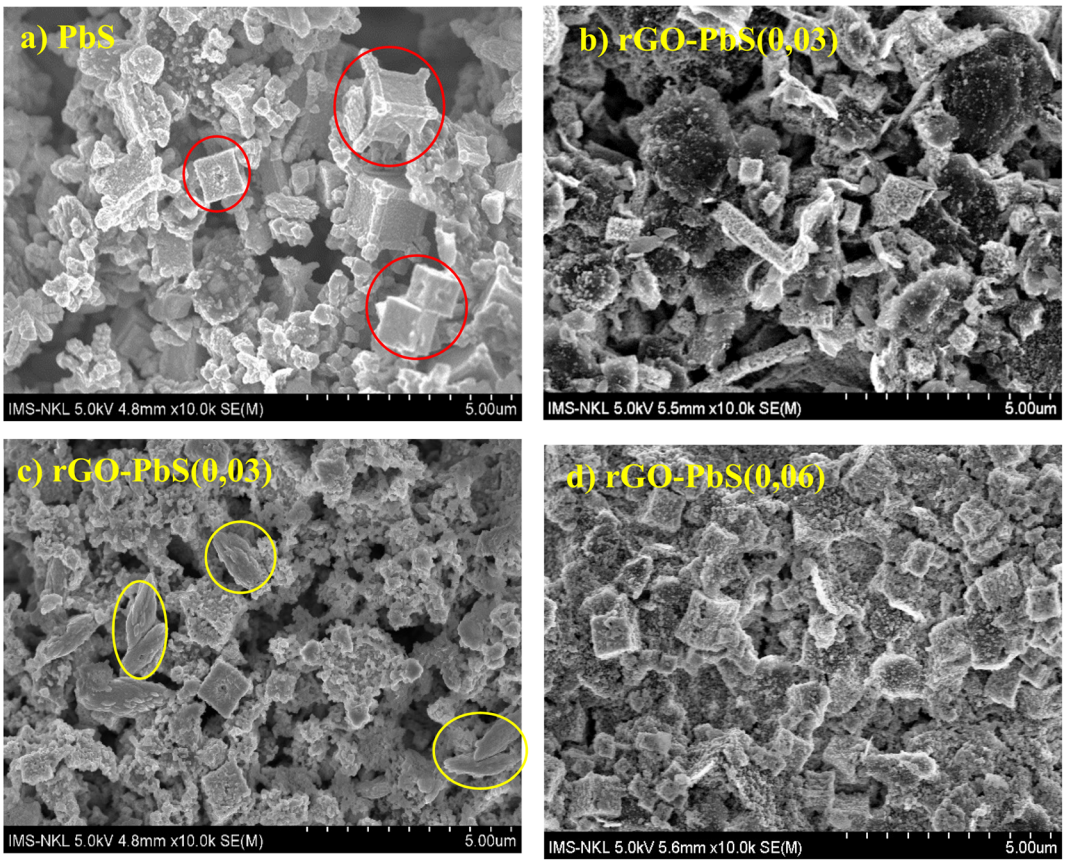

Fig. 4 FESEM images of (a) PbS, and (b–d) rGO–PbS (*x*) ($x = 0.01, 0.03, 0.06$) nanocomposites.

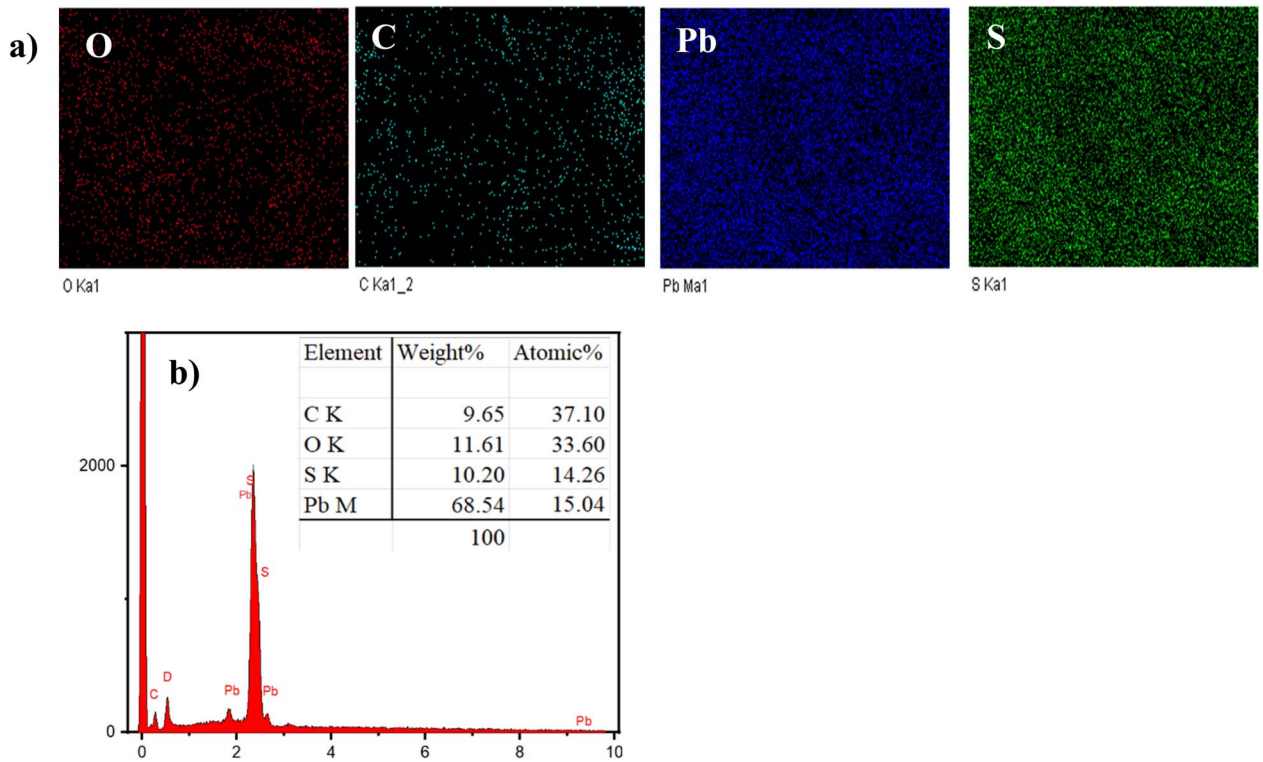

Fig. 5 (a) EDX mapping and (b) EDX spectrum of rGO–PbS (0.03) nanocomposites CE.

162.4 eV (S $2p_{1/2}$), characteristic of S^{2-} ions in Pb–S bonding. A peak at 167.5 eV, attributed to S–O bonds, which likely arise from slight oxidation or surface chemisorption.[43] The XPS data further indicate that S^{2-} ions in Pb–S bonds interact strongly with both rGO and the FTO substrate. This interaction is facilitated by the bonding of PbS with –OH groups on rGO and O^{2-}

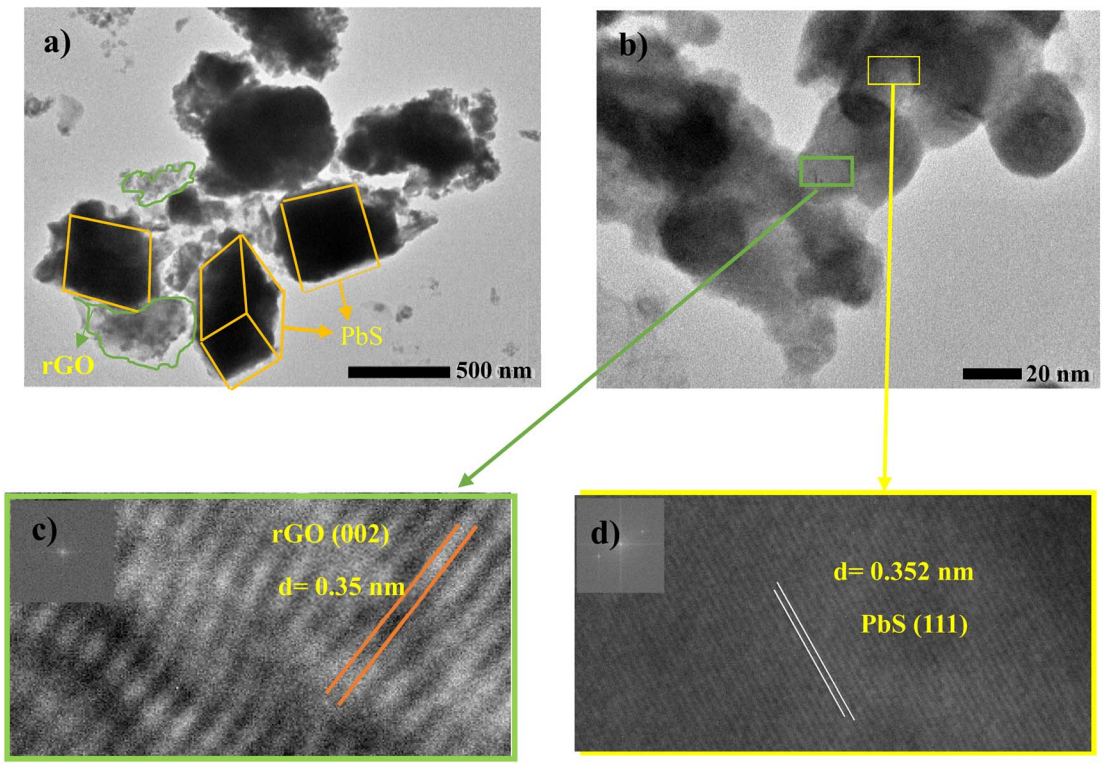

Fig. 6 (a and b) TEM and (c and d) HrTEM of rGO–PbS (0.03) nanocomposites CE.

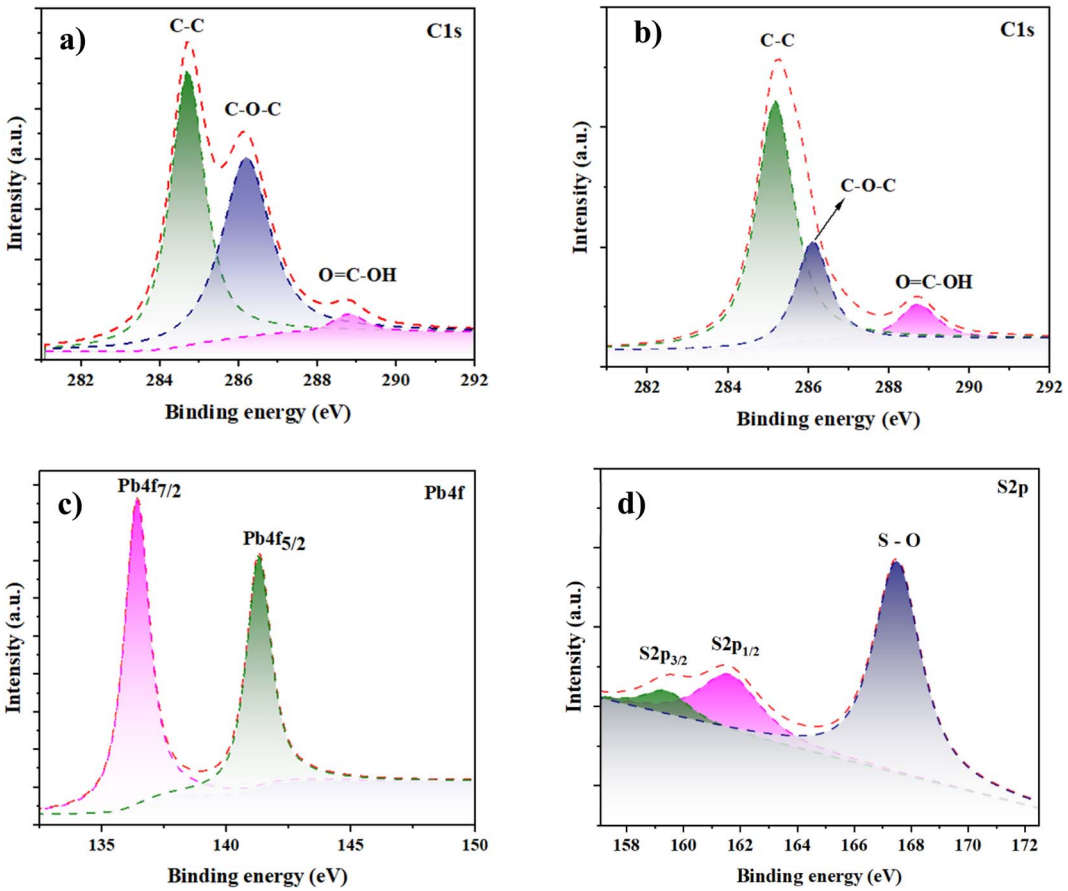

Fig. 7 High-resolution XPS (a) C 1s spectra of GO (b) C 1s (c) Pb 4f, (d) S 2p, and spectrum of rGO–PbS (0.03) nanocomposites CE.

species on the FTO surface. These robust chemical bonds enhance the mechanical stability and electrical connectivity of the counter electrode, ensuring better performance under operational conditions.

Electrochemical characterization

The construction of QDSSCs involved using PbS–rGO composite/FTO photocathodes and TiO_2 film photoanodes co-sensitized with CdS and CdSe QDs, with a polysulfide electrolyte inserted between the electrodes. *J–V* characteristic curves were measured under simulated AM1.5G solar illumination (100 mW cm^{-2}). The *J–V* curves of QDSSCs assembled with rGO, PbS, and rGO/PbS (*x*) counter electrodes are shown in Fig. 8a. Table 2 presents the corresponding photovoltaic parameters. The QDSSCs fabricated with the PbS counter electrode exhibited a power conversion efficiency (PCE) of 3.642%, short-circuit current (J_{sc}) of 17.334 mA cm^{-2}, open-circuit potential (V_{oc}) of 0.444 V, and fill factor (FF) of 0.474. As shown in Table 2, the V_{oc} and FF of the QDSSCs were significantly improved when PbS was deposited on the rGO counter electrodes compared to those of the rGO or rGO/Cu_2S counter electrodes. The increase in V_{oc} owing to the PbS CE is a p-type semiconductor (Fig. S2†), which led to an upper positive shift in qE_F compared with the redox potential of electrolytes under irradiated light.[21] Furthermore, the elevated J_{sc} and FF were ascribed to (Fig. 9) the electron moves to the electrolyte from the PbS electrode *via* two distinct pathways: electrocatalytic reduction involving S_n^{2-}/S^{2-} and injection from the PbS conduction band. The wide absorption spectrum of PbS allows it to absorb residual long-wavelength solar irradiation (Fig. S1†). The absorption process may activate PbS and enable electron transfer from the conduction band to the electrolyte. This mechanism could explain the enhanced V_{oc}, J_{sc}, and FF values observed in the rGO–PbS CE-QDSSC compared to the rGO-Cu_2S or Cu_2S CE-QDSSC (Table 1). In addition, incorporating rGO nanosheets onto the PbS nanocubic support improved the conductivity and catalytic activity for CE and enhanced photovoltaic performance. The enhanced conductivity resulting from the raised acceptor concentration of rGO–PbS (0.03) compared to PbS (Fig. S2†) indicates that the interaction between the rGO layer and PbS contributes to a higher power conversion efficiency (PCE%). The QDSSCs with the rGO–PbS (0.03) CE delivered the highest PCE (%) of 5.358%, as well as V_{oc}, J_{sc}, and FF values of 0.540 V, 21.157 mA cm^{-2}, and 0.516, respectively.

Cyclic voltammetry (CV) studies were performed to assess the effectiveness of the electrode materials in reducing the S^{2-}/S_n^{2-} electrolyte (Fig. 8b). The experiments were conducted using a three-electrode system with Pt and Ag/AgCl electrodes, in a polysulfide electrolyte containing 0.1 M S, 0.1 M Na_2S, and 0.1 M KCl, at a scan rate of 10 mV s^{-1}. The cyclic voltammetry

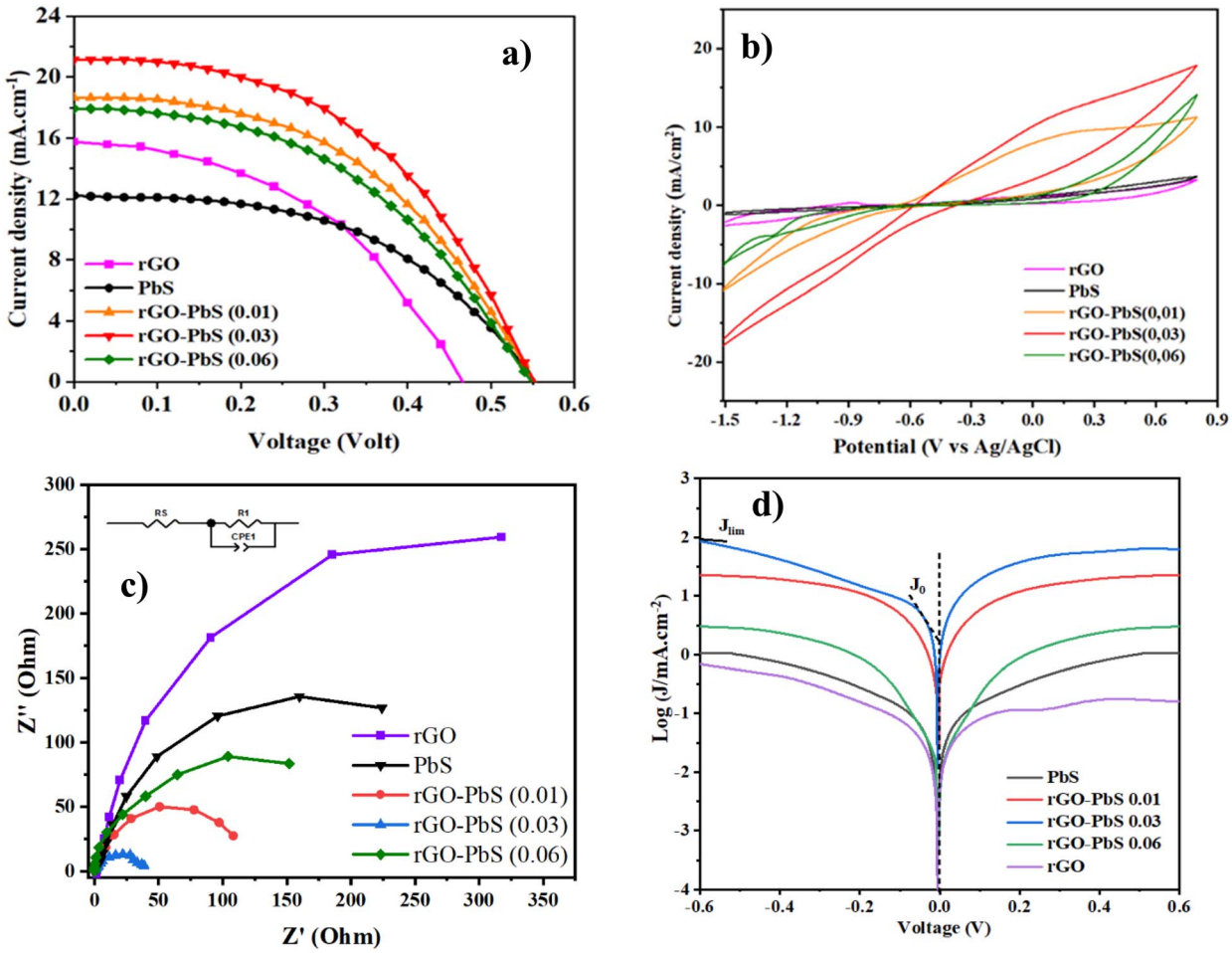

Fig. 8 (a) J–V curves; (b) CV plots; (c) Nyquist plots (inset: the equivalent circuit), and (d) Tafel polarization of PbS, GO, rGO, and rGO–PbS (x) (x = 0.01, 0.03, 0.06) electrode.

(CV) characteristics exhibit two distinct peaks: (1) the upper anodic peak arises due to the oxidation reaction, and (2) the lower cathodic peak results from the reduction reaction of S_n^{2-} to S^{2-}.[24] As shown in Fig. 8b, rGO–PbS x shows a higher reduction in current density than rGO and PbS CE. These results suggest that the composite and rGO sheets significantly enhanced the electrocatalytic capacity for polysulfide redox reduction in QDSSCs. Notably, the rGO–PbS 0.03 nanocomposite featuring rGO exhibited the highest current density owing to the improved active sites and electrical conductivity, facilitating the reduction of the S_n^{2-} to S^{2-} redox couple in the electrolyte.

To assess the catalytic performance of counter electrodes (CEs), electrochemical impedance spectroscopy (EIS) measurements were performed using a symmetric test cell containing two identical CEs. The EIS results were analyzed using Nyquist plots (Fig. 8c). The analysis employed an equivalent circuit comprising R_s, R_{ct}, and CPE. R_s denotes the series resistance between the CEs and polysulfide redox couple, while R_{ct} signifies the charge transfer resistance. CPE stands for the constant phase element. The values of R_s and R_{ct} were fitted using ZView, and the results are summarized in Table 2. The

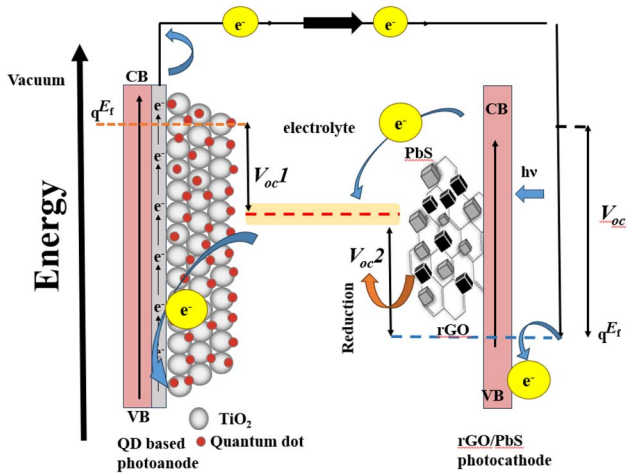

Fig. 9 Schematic structure of the QDSSC devices.

conductivity and electrocatalytic activity of counter electrodes (CEs) are critical factors that influence the performance of quantum-dot solar cells (QDSSCs). The charge transfer

Table 1 The characteristic parameters of the cell were obtained from the *J*–*V* characteristic curve and EIS spectrum

CEs	V_{oc} (V)	J_{SC} (mA cm^{-2})	FF	PCE (%)
rGO	0.440	15.758	0.477	3.311
PbS	0.540	12.226	0.507	3.349
rGO–PbS (0.01)	0.540	18.636	0.487	4.901
rGO–PbS (0.03)	0.540	21.157	0.516	5.358
rGO–PbS (0.06)	0.540	17.940	0.492	4.766
rGO/Cu_2S 24 h	0.515	20.926	0.481	5.187 (ref. 32)
Cu_2S hydro	0.480	15.226	0.412	3.012 (ref. 32)

resistance (R_{ct}) value, which reflects energy loss during electron transport at the CE/electrolyte interface, serves as a key parameter for evaluating CE efficiency. A lower R_{ct} value indicates a higher rate of electrolyte regeneration, thereby improving the overall photovoltaic performance of QDSSCs. Experimental results reveal that rGO–PbS (*x*) CEs exhibit a lower R_{ct} value compared to pure PbS CEs, largely due to the incorporation of reduced graphene oxide (rGO). Among the various compositions, the rGO–PbS (0.03) CE demonstrated the lowest R_{ct}, which can be attributed to the presence of rGO nanosheets effectively wrapping the nanocubic PbS surface. These nanosheets provide mechanical stability and establish a highly conductive framework, facilitating efficient electron transfer within the CE films. In contrast, the rGO–PbS (0.06) CE displayed a slightly higher R_{ct} value. This is likely a result of the denser morphology arising from the deposition process, which may impede charge transfer by limiting active surface area. Nonetheless, the R_s value, representing the series resistance between the CE surface and the FTO substrate, remained low across all rGO–PbS samples. This indicates good electrical contact facilitated by the rGO framework, further enhancing electron transport efficiency. Compared to the pure PbS CEs, the lower R_s and R_{ct} values of the rGO–PbS composites underscore the critical role of rGO in improving electrical conductivity and catalytic activity. These findings position rGO–PbS as a highly promising material for counter electrodes in QDSSCs, offering improved charge transfer kinetics and overall device efficiency.

Tafel polarization experiments were conducted to assess the electrocatalytic performance of the catalysts, and the results are shown in Fig. 8d. The figure illustrates three distinct zones: a low-potential polarization area, middle-potential Tafel region with a steep slope, and high-potential diffusion zone. Tafel and diffusion regions were used to evaluate the electrocatalytic capabilities of the electrodes. By extrapolating the intersections of the anodic and cathodic Tafel polarization curve branches, the exchange current density (J_0) was determined. As shown in Fig. 8d, the limiting current (J_{lim}) of the cathode intersects the vertical axis in the diffusion zone. The findings indicate that rGO–PbS (0.03) has the highest J_0 value, suggesting superior electrocatalytic activity. The remaining catalysts were ranked as follows: rGO–PbS (0.06) > rGO–PbS (0.01) > PbS > rGO. Furthermore, the J_0 value of the CE can be utilized to elucidate the charge transfer resistance ($R_{ct\text{-}Tafel}$) at the CE/electrolyte interface, as indicated in eqn (1):

$$J_0 = \frac{RT}{nFR_{ct\text{-}Tafel}} \quad (1)$$

where *R* represents the gas constant, *n* denotes the number of electrons contributing to charge transfer at the interface, *T* signifies the temperature, and *F* represents Faraday's constant.

According to eqn (1), J_0 is inversely proportional to R_{ct}; therefore, the electrochemical catalytic activity of the CE increases with increasing J_0. The $R_{ct\text{-}Tafel}$ values were in the following order: rGO–PbS (0.03) > rGO–PbS (0.06) > rGO–PbS (0.01) > PbS > rGO. The change in the $R_{ct\text{-}Tafel}$ values obtained from the Tafel plot aligns with the change in R_{ct} observed by electrochemical impedance spectroscopy (EIS). Therefore, the lower R_{ct} and $R_{ct\text{-}Tafel}$ values suggest that many electrons were transferred through the CE/electrolyte interface owing to the rapid electron transfer capability of the electrode. Furthermore, the limiting current density (J_{lim}) obtained from the diffusion of ionic carriers at the CE/electrolyte interface was directly related to the diffusion coefficient (*D*) of the S_n^{2-}/S^{2-} redox couple (eqn (2)).

$$J_{lim} = \frac{2nFCD}{l} \quad (2)$$

where *D* is the diffusion coefficient of polysulfide, and the other symbols have their usual meanings.

Fig. 8d demonstrates that the rGO–PbS (0.03) CE exhibited a higher J_{lim} than the rGO and PbS CEs, indicating an increased diffusion rate in the polysulfide electrolyte. This elevated J_{lim} value can be attributed to the higher concentration of S_n^{2-}, presumably resulting from the enhanced catalytic activity towards polysulfide reduction after PbS decoration. The data suggest that the rGO–PbS (0.06) composite exhibited superior reduction activity for S_n^{2-}, primarily because of its distinctive hierarchical structure and composite characteristics. The hierarchical structure of the catalyst confers multiple advantages. First, absorption involves both PbS and rGO, leading to an increase in the number of photoinduced electrons. Second, the hierarchical arrangement exposed a greater number of active sites. Finally, the configuration of the rGO nanosheets facilitates rapid electron conduction.

Thus far, it is evident that the enhanced electrocatalytic activity of the rGO–PbS (0.03) counter electrode (CE) significantly contributes to its superior performance in boosting power conversion efficiency (PCE). This is supported by the energy band diagram (Fig. 9), which aligns with existing literature and

Table 2 EIS characteristics were estimated from the Nyquist plots of the symmetrical cells for PbS, GO, rGO, and rGO–PbS (*x*) (*x* = 0.01, 0.03, 0.06) CEs

Sample	R_s (Ω)	R_{ct} (Ω)	CPE (μF)
PbS	29.05	578.5	0.90
rGO	31.19	602.5	0.92
rGO–PbS (0.01)	25.08	121.9	0.87
rGO–PbS (0.03)	21.29	40.15	0.71
rGO–PbS (0.06)	39.49	340.5	0.86

experimental data. Relative to the vacuum level, polysulfide (S_n^{2-}/S^{2-}) exhibits a standard reduction potential of −5.0 eV,[44] whereas the valence band of PbS is −5 eV (with the conduction band at −3.63 eV).[18] The highest occupied molecular orbital (HOMO) level of rGO was −4.82 eV (with the conduction band at −3.02 eV).[41] The HOMO level of rGO closely matches the reduction level of polysulfide, overlapping with the Fermi level (E_F) of PbS. This configuration improves the electron transfer efficiency by combining two mechanisms: rGO increases the number of accessible states near the HOMO level, thereby promoting electron movement, whereas PbS plays an active role in the reduction process. Owing to the p-type nature of PbS, its E_F is close to the valence band and equilibrates with the polysulfide reduction potential under dark conditions. In quantum dot-sensitized solar cells (QDSSCs), when electrons move from the photoanode to the CE to reduce polysulfide, the proximity of the polysulfide redox potential to the HOMO level of rGO enables a faster electron supply compared to PbS alone. This optimal band alignment minimizes the carrier loss and enhances the PCE.

4. Conclusions

In summary, the PbS–rGO composite counter electrode improves the efficiency of quantum dot-sensitized solar cells (QDSSCs). The hydrothermal synthesis process used to anchor PbS nanocubes onto reduced graphene oxide (rGO) sheets successfully yielded a composite material with superior catalytic and electrical properties. Specifically, the rGO–PbS (0.03) composite achieved the highest power conversion efficiency (PCE) of 5.358%, accompanied by an open-circuit voltage (V_{oc}) of 0.540 V, short-circuit current density (J_{sc}) of 21.157 mA cm^{-2}, and fill factor (FF) of 0.516. The presence of rGO within the composite provided an interconnected conductive framework that facilitated efficient charge transport, reduced the charge transfer resistance (R_{ct}), and improved the overall conductivity. This framework not only enhances the electrocatalytic activity of the composite but also maximizes the number of active sites available for the reduction of the S_n^{2-}/S^{2-} redox couple, as confirmed by electrochemical analyses, including cyclic voltammetry (CV) and electrochemical impedance spectroscopy (EIS). Additionally, the unique band alignment between rGO and PbS optimized the energy transfer pathway for electron movement, further contributing to the enhanced catalytic performance of the counter electrode. The hierarchical structure formed by the PbS nanocubes on the rGO sheets exposes a larger surface area and increases the absorption of incident light, enabling a more effective charge transfer mechanism at the electrode–electrolyte interface. The Nyquist and Tafel polarization plots reaffirm that the rGO–PbS (0.03) electrode exhibits significantly lower charge transfer resistance and higher exchange current density (J_0) compared to the other electrode configurations tested in this study.

Data availability

Data for this article, including origin data are available at **https://doi.org/10.6084/m9.figshare.27889173**.

Conflicts of interest

The authors declare that they have no competing financial interests or personal relationships that could influence the work reported in this study.

Acknowledgements

This work was supported by the Industrial University of Ho Chi Minh City (IUH), Ho Chi Minh, Vietnam, under grant number 23.1CB03.

References

1 J. Khan and M. H. Arsalan, *Renewable Sustainable Energy Rev.*, 2016, **55**, 414–425.
2 E. K. Solak and E. Irmak, *RSC Adv.*, 2023, **13**, 12244–12269.
3 R. Baby, P. D. Nixon, N. M. Kumar, M. S. P. Subathra and N. Ananthi, *Environ. Sci. Pollut. Res.*, 2022, **29**, 371–404.
4 N. T. K. Chung, P. T. Nguyen, H. T. Tung and D. H. Phuc, *Molecules*, 2021, **26**, 2638.
5 R. Sharif, A. Khalid, S. W. Ahmad, A. Rehman, H. G. Qutab, H. H. Akhtar, K. Mahmood, S. Afzal and F. Saleem, *Nanoscale Adv.*, 2023, **5**, 3803–3833.
6 S. Xie, X. Li, Y. Jiang, R. Yang, M. Fu, W. Li, Y. Pan, D. Qin, W. Xu and L. Hou, *Appl. Sci.*, 2020, **10**, 4285.
7 M. Halim, *Nanomaterials*, 2012, **3**, 22–47.
8 A. J. Nozik, *Phys. E*, 2002, **14**, 115–120.
9 I. R. Jo, J. A. Rajesh, Y. H. Lee, J. H. Park and K. S. Ahn, *Appl. Surf. Sci.*, 2020, **525**, 146643.
10 M. Que, W. Guo, X. Zhang, X. Li, Q. Hua, L. Dong and C. Pan, *J. Mater. Chem. A*, 2014, **2**, 13661.
11 Z. Tian, Q. Chen and Q. Zhong, *Chem. Eng. J.*, 2020, **396**, 125374.
12 C. V. V. M. Gopi, S. Srinivasa Rao, S.-K. Kim, D. Punnoose and H.-J. Kim, *J. Power Sources*, 2015, **275**, 547–556.
13 M. P. A. Muthalif and Y. Choe, *J. Colloid Interface Sci.*, 2021, **595**, 15–24.
14 V. H. Vinh Quy, J.-H. Kim, S.-H. Kang, C.-J. Choi, J. A. Rajesh and K.-S. Ahn, *J. Power Sources*, 2016, **316**, 53–59.
15 J. Wang, Md. M. Rahman, C. Ge and J.-J. Lee, *J. Ind. Eng. Chem.*, 2018, **62**, 185–191.
16 Q. Pei, Z. Chen, S. Wang, D. Zhang, P. Ma, S. Li, X. Zhou and Y. Lin, *Sol. Energy*, 2019, **178**, 108–113.
17 E. P. Gür, M. Eryiğit and Ü. Demir, *Electrochim. Acta*, 2023, **438**, 141584.
18 M. Muhyuddin, T. F. Khan, M. A. Akram, I. Ali, T. J. Park and M. A. Basit, *J. Photochem. Photobiol., A*, 2020, **400**, 112720.
19 T. Xu, J. Hu, P. Wei, X. Qin, T. Huang, L. Chen and H. Wu, *Funct. Mater. Lett.*, 2018, **11**, 1850025.
20 N. Van Le, H. T. Nguyen, H. V. Le and T. T. P. Nguyen, *J. Electron. Mater.*, 2017, **46**, 274–281.
21 C. Y. Lin, C. Y. Teng, T. L. Li, Y. L. Lee and H. Teng, *J. Mater. Chem. A*, 2013, **1**, 1155–1162.
22 S. S. Rao, I. K. Durga, C. V. Tulasi-Varma, D. Punnoose, L. J. Cheol and H.-J. Kim, *New J. Chem.*, 2015, **39**, 7379–7388.

23 B. Van Thang, H. T. Tung, D. H. Phuc, T. P. Nguyen, T. Van Man and L. Q. Vinh, *Sol. Energy Mater. Sol. Cells*, 2023, **250**, 112042.
24 W. Li, S. Zhang, Q. Chen and Q. Zhong, *Chem. Eng. J.*, 2022, **430**(Part 1), 132732.
25 W. Li, S. Zhang, Q. Chen and Q. Zhong, *Catal. Sci. Technol.*, 2021, **11**, 2745–2752.
26 P. Parand, M. Samadpour, A. Esfandiar and A. Iraji Zad, *ACS Photonics*, 2014, **1**, 323–330.
27 Y. Yang, L. Zhu, H. Sun, X. Huang, Y. Luo, D. Li and Q. Meng, *ACS Appl. Mater. Interfaces*, 2012, **4**, 6162–6168.
28 M. Samadpour and S. Arabzade, *J. Alloys Compd.*, 2017, **696**, 369–375.
29 Q. Pei, Z. Chen, S. Wang, D. Zhang, P. Ma, S. Li, X. Zhou and Y. Lin, *Sol. Energy*, 2019, **178**, 108–113.
30 A. Ramesh, M. Jeyavelan and M. S. Leo Hudson, *Dalton Trans.*, 2018, **47**, 5406–5414.
31 R. Amin, P. Ramesh Kumar and I. Belharouak, in *Carbon Nanotubes - Redefining the World of Electronics*, IntechOpen, 2021.
32 N. T. My Hanh, H. T. Tung, N. T. K. Duyen, V. C. Nguyen, L. Van Hieu, N. T. Nguyen and H. P. Dang, *Ceram. Int.*, 2024, **50**(15), 27127–27138.
33 L. N. Maskaeva, A. V. Pozdin, A. Yu. Pavlova, Yu. V. Korkh, T. V. Kuznetsova, V. I. Voronin, K. E. Krivonosova, T. B. Charikova and V. F. Markov, *Phys. Chem. Chem. Phys.*, 2024, **26**, 10641–10649.
34 K. Paulraj, S. Ramaswamy, I. S. Yahia, A. M. Alshehri, H. H. Somaily, H.-S. Kim and A. Kathalingam, *Appl. Phys. A:Mater. Sci. Process.*, 2020, **126**, 503.
35 W. Li, G. Long, Q. Chen and Q. Zhong, *J. Power Sources*, 2019, **430**, 95–103.
36 B. Heidari, A. Majdabadi, L. Naji, M. S. Ghamsari, Z. Fakharan and S. Salmani, *Opt. Quantum Electron.*, 2018, **50**, 267.
37 B. D. Ossonon and D. Bélanger, *RSC Adv.*, 2017, **7**, 27224–27234.
38 D. R. Dreyer, S. Park, C. W. Bielawski and R. S. Ruoff, *Chem. Soc. Rev.*, 2010, **39**, 228–240.
39 M. S. Bakshi, P. Thakur, S. Sachar, G. Kaur, T. S. Banipal, F. Possmayer and N. O. Petersen, *J. Phys. Chem. C*, 2007, **111**, 18087–18098.
40 A. V Borhade and B. K. Uphade, *A Comparative Study on Characterization and Photocatalytic Activities of Pbs and Co Doped Pbs Nanoparticles*, 2012, vol. 9.
41 A. R. Lara-Canche, V. Vinayakumar, D. F. Garcia-Gutierrez, E. Martinez-Guerra and D. I. Garcia-Gutierrez, *J. Alloys Compd.*, 2023, **932**, 167707.
42 L. Stobinski, B. Lesiak, A. Malolepszy, M. Mazurkiewicz, B. Mierzwa, J. Zemek, P. Jiricek and I. Bieloshapka, *J. Electron Spectrosc. Relat. Phenom.*, 2014, **195**, 145–154.
43 S. Monika, M. Mahalakshmi, N. Subha, M. S. Pandian and P. Ramasamy, *Diamond Relat. Mater.*, 2022, **125**, 109033.
44 D. Ghosh, G. Halder, A. Sahasrabudhe and S. Bhattacharyya, *Nanoscale*, 2016, **8**, 10632–10641.